Modelling-assisted geometrical optimization of colloidal quantum color convertor based pixels fabricated by dielectrophoretic directed assembly

Priyanka Tyagi, Etienne Palleau, Laurence Ressier, Michele d'Amico, Yu-Pu Lin, Omid Faizy, Martine Meireles, Yannick Hallez

Graphical Abstract

Modelling-assisted geometrical optimization of colloidal quantum color convertor based pixels fabricated by dielectrophoretic directed assembly

Priyanka Tyagi, Etienne Palleau, Laurence Ressier, Michele D'Amico, Yu-Pu Lin, Omid Faizy, Martine Meireles, Yannick Hallez

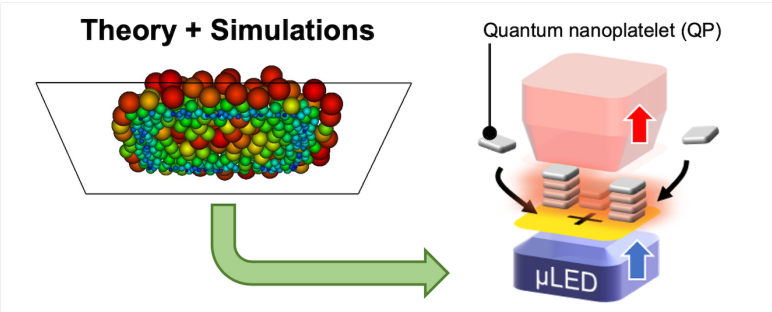

Modelling-assisted geometrical optimization of colloidal quantum color convertor based pixels fabricated by dielectrophoretic directed assembly

Priyanka Tyagi[a,b], Etienne Palleau[a], Laurence Ressier[a], Michele D'Amico[b], Yu-Pu Lin[b], Omid Faizy[c], Martine Meireles[c], Yannick Hallez[c]

[a]*LPCNO, Université de Toulouse, CNRS, INSA, UPS, 135 avenue de Rangueil, Toulouse, 31077, France*
[b]*NEXDOT, 102 Av. Gaston Roussel, Romainville, 93230, France*
[c]*Laboratoire de Génie Chimique, Université de Toulouse, CNRS, INPT, UPS, Toulouse, France*

Abstract

Hypothesis: Building competitive color conversion pixels for microdisplays made of semiconductor nanocrystals requires reaching a deposition thickness high enough to absorb all the blue light from the backlight unit. In the case of dielectrophoretic directed assembly of such nanocrystals, modeling and simulations may help understand what the intrinsic limitations of the process are, and may be used to propose new assembly routes.

Experiments: A theoretical model of dielectrophoretic interactions between polarizable nano-spheres and an electrostatically patterned substrate has been developed. Monte Carlo simulations have been run using this model to rationalize the effects of parameters driving the dielectrophoretic directed assembly and to find optimal deposition conditions for reaching a maximal thickness of nanocrystal pixels. Experiments with CdSe quantum plates and with alumina spheres embedding quantum plates (micro-pearls) have been carried out and compared to the model.

Findings: Modeling and simulations reveal that the directed assembly of semiconductor nanocrystals is limited essentially by the small object size, which sets the maximum dielectrophoretic force they can undergo. They indicate that using larger objects should allow reaching unprecedented assembly heights, but will induce lateral extension of the assembly. This trade-off has been illustrated with diagrams in the parameter space and confirmed experimentally with micro-pearls.

Keywords: Modeling, Simulation, Monte Carlo, Nanoxerography, Assembly, Electrostatic, Dielectrophoresis, Quantum dot, Quantum plate, Display
PACS: 0000, 1111
2000 MSC: 0000, 1111

Recent display technologies can produce high quality colors using semiconductor nanocrystals (SNCs) such as quantum dots, rods or plates. The general principle is to convert UV/blue light emitted from a backlight unit by light-emitting diodes into pure red and green when it passes through a SNC layer [1, 2, 3, 4]. Commercially available displays using SNCs are based on the first generation quantum dot (QD) technology in which QDs are distributed uniformly in a polymer matrix called quantum dot enhancement film or color enhancement film (QDEF). Due to their unique tunable optical properties, SNCs absorb UV/blue light coming from the backlight unit and convert it into narrow red and green (R/G) emission spectra to make purer white light. It is further combined to color filters and a liquid-crystal display to generate R/G/B subpixels. However, this technology presents two main limitations: the color filters absorb about 2/3 of the incident light and the large QDEF surface area requires incorporating a large quantity of expensive SNCs.

Significant performance enhancement and cost reduction are expected with the second generation QD technology based on quantum dot color converters (QDCC): instead of using a uniform color enhancement film, the idea is to deposit the R/G emitting nanocrystals exactly and only at the positions of future R/G/B subpixels [1, 3]. Using such a patterned QD array, the quantity of SNCs required is significantly reduced and a tripling of the light efficiency may be expected by removing the now useless color filters. Other demonstrated advantages are a wider color gamut and a wider viewing angle. Furthermore, higher pixel resolution is also expected, allowing to access new applications in microdisplays [2, 5]. Because the external conversion efficiency (number of blue photons converted to red/green divided by total number of blue photons sent through the subpixel) should be as high as 95% for QDCC-based displays, maximizing the number of quantum dots assembled on each pixel is of paramount importance.

Recent realizations of QDCC have been possible using various structuring techniques, mainly inkjet printing and photolithography which both present different pros and cons. Inkjet printing allows to create QD arrays without waste but high lateral resolution is difficult to achieve. Photolithography can

tackle this limitation but the embedded QDs need high chemical resistance [3, 6]. Nanoxerography is an alternative method allowing to achieve high resolution without the aforementioned drawbacks [7, 8, 9]. It is a directed electrostatic assembly technique similar to the technology used in laser printers but performed at the nanoscale and in a liquid. This versatile method has already been used to assemble different colloidal nano-objects on well defined, (sub)micron-scale patterns [10, 11, 12]. The principle of nanoxerography is to create charged patterns of controlled geometry in an electret substrate, and to employ them as electrostatic traps to capture nano-objects of interest at the desired locations. Charged patterns can be created by applying a strong electric field on the substrate locally, for example using, among multiple techniques, ion [13, 14, 15] or electron [13, 16] beams, a conducting micro-structured stamp (electrical micro-contact printing) [17, 18] or with a conducting atomic force microscope (AFM) tip [19, 20, 21, 22, 23, 24, 7]. Among these approaches, AFM nanoxerography is very versatile as it allows changing the pattern geometry and charge at no cost and on the same substrate. It also allows for an immediate characterization of the injected charges using Kelvin probe force microscopy (KFM) with the same tip. It is therefore very useful for prototyping and reaching high resolution patterns. Foreseen advantages of nanoxerography compared to alternative structuring techniques are an increased spatial resolution in the range of thousands of pixels-per-inch compatible with the pixel size of micro-LED displays, scalability thought electrical micro-contact printing, and the use of mild physico-chemical conditions.

In recent works, potentialities of nanoxerography for display applications were demonstrated by a creating cm^2 large array of 3 µm wide and 60-120 nm thick assemblies made of close-packed 20 nm wide Core-Shell Cd(Se,S)/(Cd,Zn)S red and green quantum plates (QPs) and conversion characterizations on active µLED matrices were performed [10, 25]. One remaining issue is that the corresponding light conversion efficiency is still too low for the technology to be implemented in commercial displays. Besides improving the intrinsic conversion efficiency of SNC themselves, obtaining a higher conversion rate requires increasing the SNC layer thickness and the SNC density inside this layer. Clearly, building thick color converter SNC based assemblies is mandatory.

In nanoxerography, in order to create such thick 3D assemblies by electrostatic driven directed assembly, diectrophoretic forces (DEP) has to be predominant over all other forces. This is possible in the case of non-charged but polarizable colloidal systems dispersed in non polar solvents [26].

The objectives of the present work are to develop models and simulations to understand why recent attempts at building patterned color conversion layers using nanoxerography could only produce assemblies with thicknesses lower than 150-200 nm and to propose new assembly routes.

A model to compute the electrostatic interaction energy of spherical nanoparticles in the electric field generated by an array of charged regions is proposed in section 1. Results of Monte Carlo simulations, semi-analytical predictions for nanoparticle assembly height based on this interaction

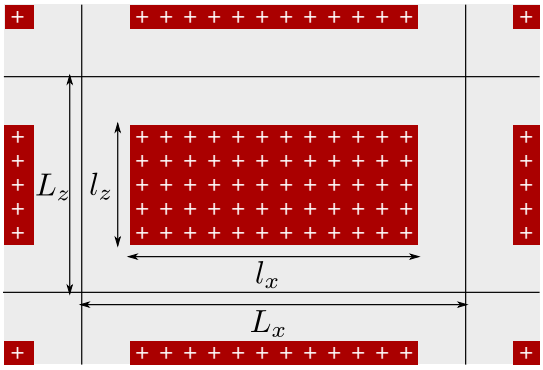

Figure 1: Geometry of the charge pattern imprinted in the electret substrate.

model, and nanoxerography experiments conducted with quantum plates are then discussed in section 2. The option of embedding small SNCs into larger monodisperse colloidal carriers is evaluated with theory and simulations in section 3. Experiments with real, polydisperse colloidal carriers are discussed in light of the theoretical results and recommendations for future assembly experiments are proposed in section 4.

1. Modeling

The electric fields for the present application are DC fields. The polar solvent and the semiconductor nanoparticles are considered as perfect dielectrics. Nanoparticles are modeled as spheres of radius a and static dielectric constant ϵ_s immersed in a fluid of static dielectric constant ϵ. The substrate is in the (x, z) plane and patterned with a periodic array of rectangular charged regions centered over each subpixel (see Fig. 1). The dimensions of each charged area in the x and z directions are denoted l_x and l_z. The periodicity of the array of charged regions, which is also the subpixel pitch, is denoted L_x in the x direction and L_z in the z direction. Note that in AFM nanoxerography, to create the charged area at the center of each subpixel, the AFM tip scans the area along x and z and performs local charge injections until the full subpixel is covered by a discrete sub-pattern of injection "points". The size of these points is typically a few tens of nanometers and their spacing is about 100–200 nm. Depending on the substrate material, environmental conditions, and AFM tip geometry, the charged regions associated to each injection point may have very sharp boundaries or appear more Gaussian-like due to diffusion of the injected charges in the substrate. In the theoretical model presented here the local potential fluctuations associated to the discrete injection points will be ignored to keep the electrostatics problem tractable. We will only consider a uniform, average surface potential over the entire charged region surface. Hereafter, this approximation will prove to be sufficient to predict the correct nanoparticle assembly thickness as a function of the nanoxerography process parameters, although some details of the nanoparticle distribution over the subpixel surface will be lost.

If the curvature of the electric field $\vec{E}(\vec{x})$ is small enough to assume local gradient uniformity at the scale of a sphere hovering above the substrate, the force exerted on a polarized sphere

at position $\vec{x}$ can be approximated by

$$\vec{F} = \vec{p} \cdot \nabla \vec{E} \tag{1}$$

and its potential energy is

$$U = -\frac{1}{2}\vec{p} \cdot \vec{E}, \tag{2}$$

where $\vec{p}$ is an effective dipole given by

$$\vec{p} = 4\pi\epsilon K a^3 \vec{E} \tag{3}$$

and $K = (\epsilon_s - \epsilon)/(\epsilon_s + 2\epsilon)$ is the Clausius-Mossotti factor expression relevant for ideal dielectrics [27, 28]. More precise models can be built with numerical simulations or multipole expansions if necessary. In particular, we solved the Laplace equation for the 3D electric potential field inside and around a sphere above a charged pattern numerically and integrated the Maxwell stress tensor on the nano-object surface to get exact DEP forces as a function of substrate-colloid distance. The numerical method, already used in previous works [29, 30], accounts for the dielectric jump at the surface of nano-objects exactly, and is thus equivalent to calculating all the terms in a multipole expansion. Results are compared to the dipole approximation in Supplementary Material. The difference is always less than 10% for the conditions relevant for this work.

The next step to use relations (1) or (2) in simulations is to compute the background electric field $\vec{E}$ generated by the charged substrate. Dielectrophoretic assembly experiments are usually conducted in non-polar solvents such as octane, so the Bjerrum length is very important and any ionic species of a given charge would be immediately condensed with species of opposite charge to form neutral objects. Therefore, there are no free charges in the solvent above the substrate and the electric potential ψ obeys the Laplace equation $\Delta\psi = 0$. For the doubly periodic array of subpixels under investigation, the analytical solution for ψ can be found by expanding both ψ and the boundary conditions in double Fourier cosine series. The general form of the potential is

$$\psi(x, y, z) = \sum_{m=0}^{\infty}\sum_{n=0}^{\infty} B_{mn}(y)\cos(\nu_n x)\cos(\mu_m z), \tag{4}$$

where $\nu_n = 2\pi n/L_x$ and $\mu_m = 2\pi m/L_z$. When inserted in the Laplace equation, this leads to

$$B''_{mn}(y) - \lambda_{mn}^2 B_{mn}(y) = 0, \tag{5}$$

where $\lambda_{mn}^2 = \nu_n^2 + \mu_m^2$. The coefficient B_{00} can in principle be linear in y, but it will actually simply be constant for the boundary conditions used here. Other coefficients B_{mn} are the combination of $e^{+\lambda_{mn}y}$ and $e^{-\lambda_{mn}y}$ functions. Solutions that must vanish away from the substrate ($y \to \infty$) are of the general form

$$\psi(x, y, z) = \sum_{m=0}^{\infty}\sum_{n=0}^{\infty} \delta_{mn}\cos(\nu_n x)\cos(\mu_m z)e^{-\lambda_{mn}y}. \tag{6}$$

The δ_{mn} coefficients depend on the desired surface potential distribution. Here the surface potential is considered fixed at a value A inside the rectangle defined by $|x| < l_x/2$ and $|z| < l_z/2$, whereas it is 0 elsewhere. For simplicity, A will be called "subpixel potential" hereafter. Expanding this boundary condition on the substrate yields

$$\begin{aligned}\psi|_{y=0} =& A\frac{l_x}{L_x}\frac{l_z}{L_z}\left[1 + \sum_{n=1}^{\infty} A_n\cos(\nu_n x) + \sum_{m=1}^{\infty} B_m\cos(\mu_m z)\right.\\ &\left. + \sum_{m=1}^{\infty}\sum_{n=1}^{\infty} A_n B_m\cos(\nu_n x)\cos(\mu_m z)\right],\end{aligned} \tag{7}$$

where

$$\begin{cases} A_n &= 2\mathrm{sinc}(\nu_n l_x/2), \\ B_m &= 2\mathrm{sinc}(\mu_m l_z/2). \end{cases} \tag{8}$$

Matching equation (6) with $y = 0$ and equation (7) allows to determine the δ_{mn} coefficients and thus the electric potential

$$\begin{aligned}\psi(x, y, z) =& A\frac{l_x}{L_x}\frac{l_z}{L_z}\left[1 + \sum_{n=1}^{\infty} A_n\cos(\nu_n x)e^{-\nu_n y} + \sum_{m=1}^{\infty} B_m\cos(\mu_m z)e^{-\mu_m y}\right.\\ &\left. + \sum_{m=1}^{\infty}\sum_{n=1}^{\infty} A_n B_m\cos(\nu_n x)\cos(\mu_m z)e^{-\lambda_{mn}y}\right]\end{aligned} \tag{9}$$

and the electric field

$$\begin{aligned}\vec{E}(x, y, z) =& A\frac{l_x}{L_x}\frac{l_z}{L_z}\left[\sum_{n=1}^{\infty}\nu_n A_n e^{-\nu_n y}\begin{pmatrix}\sin(\nu_n x)\\ \cos(\nu_n x)\\ 0\end{pmatrix}\right.\\ &+ \sum_{m=1}^{\infty}\mu_m B_m e^{-\mu_m y}\begin{pmatrix}0\\ \cos(\mu_m z)\\ \sin(\mu_m z)\end{pmatrix}\\ &\left.+ \sum_{m=1}^{\infty}\sum_{n=1}^{\infty} A_n B_m e^{-\lambda_{mn}y}\begin{pmatrix}\nu_n\sin(\nu_n x)\cos(\mu_m z)\\ \lambda_{mn}\cos(\nu_n x)\cos(\mu_m z)\\ \mu_m\cos(\nu_n x)\sin(\mu_m z)\end{pmatrix}\right]\end{aligned} \tag{10}$$

In the special case of a square array with $l_x = l_z \equiv l$ and $L_x = L_z \equiv L$, the ratio $\theta = l/L$ is the only dimensionless parameter appearing in the electric field, and we have $\nu_k = \mu_k$ and $A_k = B_k$. So the electric field scaled by A/l can be written

$$\begin{aligned}\vec{\tilde{E}} =& \sum_{m=1}^{\infty} 4\theta^2\sin(\pi m\theta)e^{-2\pi m\theta\bar{y}}\begin{bmatrix}\sin(2\pi m\theta\bar{x})\\ \cos(2\pi m\theta\bar{x}) + \cos(2\pi m\theta\bar{z})\\ \sin(2\pi m\theta\bar{z})\end{bmatrix}\\ &+ \sum_{m=1}^{\infty}\sum_{n=1}^{\infty}\frac{8\theta}{\pi mn}\sin(\pi n\theta)\sin(\pi m\theta)e^{-2\pi\sqrt{m^2+n^2}\theta\bar{y}}\\ &\times\begin{bmatrix}n\sin(2\pi n\theta\bar{x})\cos(2\pi m\theta\bar{z})\\ \sqrt{m^2+n^2}\cos(2\pi n\theta\bar{x})\cos(2\pi m\theta\bar{z})\\ m\cos(2\pi n\theta\bar{x})\sin(2\pi m\theta\bar{z})\end{bmatrix}\end{aligned} \tag{11}$$

where coordinates with an overbar are scaled by the size l of the charged area. When these square regions are separated by distances equal to their own size (as for R/G/B subpixels organized as 2×2 square arrays), the factor θ is 1/2, allowing further simplification. In this case $\sin(m\pi\theta)$ reduces to 0 if m is even or $(-1)^p$ if $m = 2p + 1$. The electric field for such a subpixel array

is then

$$\vec{\bar{E}}|_{\theta=1/2} = \sum_{p=0}^{\infty}(-1)^p e^{-(2p+1)\pi\bar{y}} \begin{bmatrix} \sin(\pi(2p+1)\bar{x}) \\ \cos(\pi(2p+1)\bar{x}) + \cos(\pi(2p+1)\bar{z}) \\ \sin(\pi(2p+1)\bar{z}) \end{bmatrix}$$
$$+ \sum_{p=0}^{\infty}\sum_{q=0}^{\infty} \frac{4(-1)^p(-1)^q}{\pi(2p+1)(2q+1)} e^{-\pi\sqrt{(2p+1)^2+(2q+1)^2}\bar{y}}$$
$$\times \begin{bmatrix} (2q+1)\sin(\pi(2q+1)\bar{x})\cos(\pi(2p+1)\bar{z}) \\ \sqrt{(2p+1)^2+(2q+1)^2}\cos(\pi(2q+1)\bar{x})\cos(\pi(2p+1)\bar{z}) \\ (2p+1)\cos(\pi(2q+1)\bar{x})\sin(\pi(2p+1)\bar{z}) \end{bmatrix} \quad (12)$$

This expression will prove to be useful later.

The general solution (10) was used with equations (2) and (3) to perform Monte Carlo simulations of nanoparticle assembly. Note that in this case, in calculating an energy on a specific particle we ignore perturbations of the electric field stemming from the presence of all other particles in the domain. It means that we neglect the induced-dipole-induced-dipole interactions between nano-objects. These interactions are an order of magnitude smaller that the charged-pattern-colloid interactions and including them is not necessary to observe good agreement between simulations and experiments as will be shown later.

The simulations were run in a box periodic along the x and z dimensions, with lateral extents L_x and L_z, and of height $2h$. It contained a single subpixel. In order to mimic a charged region in contact with a very large reservoir of colloids, we used a Grand Canonical Monte Carlo (GCMC) algorithm which sets the bulk density of colloids to a value ρ_b. During each MC cycle, attempts to move, insert, or delete colloids were made. Equilibrium was considered to be reached when the number of colloids in the box and the total potential energy were stabilized. Simulations were run for both monodisperse and polydisperse suspensions. When trying to insert a new colloid from a polydisperse suspension, its size was chosen randomly in a truncated log-normal distribution reproducing experimental size polydispersity (more details in section 4).

The geometrical and chemical parameters of the simulations were taken around a reference configuration chosen close to experiments. Parameters of this reference case are reported in Table 1. The solid phase permittivity value ϵ_s corresponds to CdSe, CdZnS, and alumina, which are the materials constituting the quantum plates and micropearls used in the experiments. The liquid phase permittivity value ϵ corresponds to octane. The subpixel potential $A = 7\,V$ is set to a value typically encountered in nanoxerography. The subpixel dimensions $l_x = l_z$ and periodicity $L_x = L_z$ are in the lower range of micro-LED displays. The nano-particle bulk density ρ_b and size distribution parameters a_m, a_{std} and $a_{\max}$ were determined experimentally (section 4). The number of terms considered in the double sums of section 1, $n_{\max}$, has been chosen by testing larger and larger values until the results became independent of $n_{\max}$. Throughout the article, the simulation control parameters are set to the values reported in Table 1 unless specified otherwise.

In the next sections, this modeling framework is used to discuss the assembly of single nanocrystals, larger canonical monodisperse colloidal carriers, and finally real polydisperse realizations of such carriers.

Table 1: Parameters used in the reference case. ϵ_s, ϵ, and ϵ_0 are the colloid, solvent, and vacuum permittivities, respectively. A is the surface potential of the charged patterns, or subpixel potential. L_x and L_z are the charge pattern periodicity (or pitch) in the x and z directions. l_x and l_z are the subpixel dimensions in the x and z directions. ρ_b is the nanoparticle number density in the bulk suspension. For polydisperse suspensions, a_m is the mean colloidal radius, a_{std} is the standard deviation of colloidal radii, and $a_{\max}$ is the maximum allowed colloid radius. $n_{\max}$ is the number of terms included in sums of section 1.

Quantity	Value	Unit
ϵ_s	$9\epsilon_0$	$F.m^{-1}$
ϵ	$1.95\epsilon_0$	$F.m^{-1}$
A	7	V
$L_x = L_z$	10	μm
$l_x = l_z$	5	μm
ρ_b	2.417×10^{17}	m^{-3}
a_m	150	nm
a_{std}	66	nm
$a_{\max}$	350	nm
$n_{\max}$	128	

2. Assembly of monodisperse nanocrystals

The goal of the first set of simulations was to understand why the thickness of assemblies of CdSeS/CdS/ZnS core-shell-shell quantum plates with dimensions 10 nm×20 nm×20 nm never exceeded 150-200 nm in previous nanoxerography experiments despite several optimization attempts [10, 25]. To this end, we first verified that the quantum plates could be coarse-grained as spheres with the same volume: detailed calculations showed that the forces exerted on these two types of nano-objects differ by less than 17% in the conditions investigated here (see Supplementary Material).

Simulations have first been run for radii ranging from 10 to 200 nm and subpixel potentials ranging from 0.5 to 10 V. Maps of assembly height were computed at equilibrium and are reported as a function of nanoparticle radius in Fig. 2a for radii up to 120 nm. For small radii and small subpixel potentials, nanoparticles assemble only on the edges of the charged regions in the simulations. As the radius and subpixel potential increase, the width of the assembly increases. This evolution is more marked for a radius increase than for a potential increase. At some point, nanoparticles start to assemble on the whole charged region surface but the assembly is still thicker over the edges of these regions. For even larger particle radii, the maximum assembly height is found at the subpixel center and it can be as large as 2.4 µm for a 120 nm radius and a subpixel potential of 7 V in the conditions of Fig. 2. Eventually, for large enough radii the assemblies of neighbouring subpixels begin to merge. This sequence can be explained by the fact that the DEP force depends on the electric field gradient, which is larger on the edges of the charged regions due to the potential discontinuity. For very small particles, the dipole moment is small (it scales as a^3), so only the zone around the edge of the charged region with the most intense ∇E^2 allows to reach attraction energies comparable to the thermal energy. For larger and larger particles, reaching the energy threshold for assembly is possible

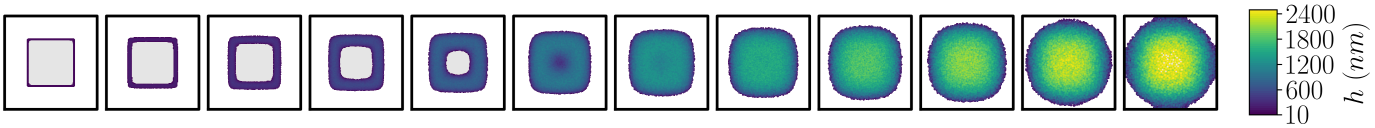

(a) Radii range from 10 to 120 nm by steps of 10 nm, from left to right, with $A = 7\,V$.

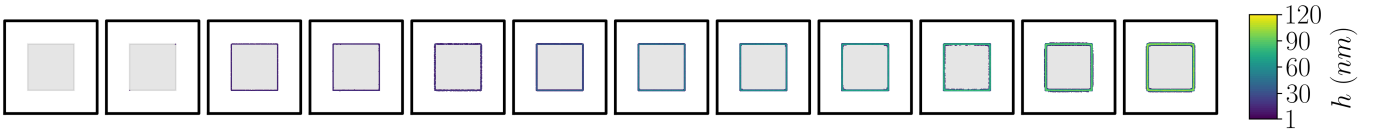

(b) Subpixel potentials A take values 1, 1.5, 2, 2.5, 3, 4, 5, 6, 7, 8, 9 and 10 V from left to right, with $a = 10\,nm$.

Figure 2: Assembly height map in Monte Carlo simulations of monodisperse suspensions. The charged region is shaded. The parameters used here are those reported in Table 1 unless specified otherwise.

for weaker and weaker ∇E^2 so particles can deposit away from the edges of charged regions. The largest particles can also respond to the relatively weak gradient of E_y^2 above the subpixel center, which explains why their assembly is effective all over the surface of charged regions. The reason why a maximum thickness can be observed at pixel centers for larger colloids is discussed in Supplementary Material. With these arguments at hand, one may anticipate that in experiments the local subpixel potential fluctuations due to the discrete injection points may induce local values of ∇E^2 close to the surface large enough to assemble nanoparticles over the full charged region surface, but that the assembly thickness predicted over the edges of the charged regions should be correct because ∇E^2 there will be similar in simulations and experiments.

Maps of assembly height for a small particle radius fixed at 10 nm, which is typical for light-emitting nanocrystals, and subpixel potentials varying between 1 and 10 V are reported in Fig. 2b. No assembly is observed below 1 V and only assembly on subpixel edges is observed for larger potentials. Moreover, the maximum assembly height obtained at A =10 V is only about 120 nm for such small objects.

More insight can be obtained by comparing these results with (semi-)analytical predictions. The nanoparticle assembly height at a specific point (x, z) on the substrate can be estimated as the position $y = h_c$ above the substrate such that the electrostatic interaction energy (2) balances some critical thermal energy value ηkT:

$$U(x, z, h_c) = \eta kT. \tag{13}$$

Here we use $\eta = 15$, a value often reported as the critical threshold for colloidal stability [31]. Solving this equation for h_c is possible numerically anywhere on the substrate using expression (10). Note that the assembly height is rigorously defined by energetic considerations such as (13), but color conversion capabilities of QP assemblies are discussed more easily in terms of average number of QPs that a photon can encounter while passing through the assembly. Calculating this number precisely is not possible because it depends on the density and arrangement of QPs inside the assembly, which depends in turn on the nanoxerography process parameters [10]. Previous microscopy observations showed a first layer of QPs lying flat on

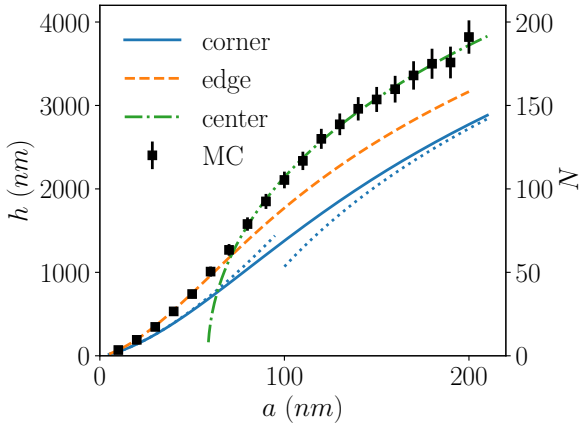

(a) Assembly height h as a function of particle radius a for a subpixel potential $A = 7\,V$.

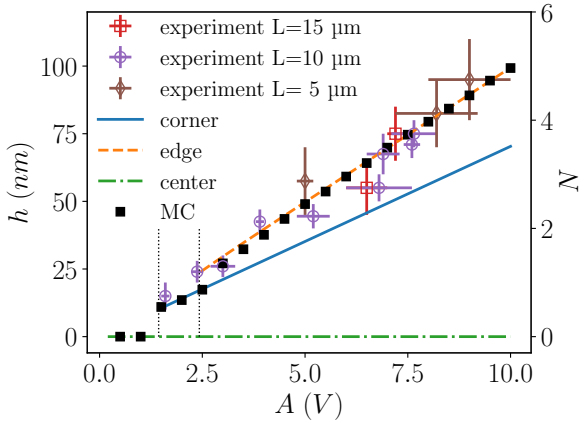

(b) Assembly height h as a function of subpixel potential A for a particle radius $a = 10\,nm$.

Figure 3: Assembly height h in Monte Carlo simulations (maximum value) and as predicted by theory at the corner, edge, and center of charged regions. The dotted lines are the simple solutions (19) and (20). The parameters used here are those reported in Table 1 unless specified otherwise. Open symbols are used for experiments with quantum plates assembled on arrays of subpixels with periodicity $L = 5\,\mu m$ (◊), $10\,\mu m$ (○), and $15\,\mu m$ (□).

the substrate surface, and loosely packed QPs with quite random orientations above. Therefore, in what follows the assembly height will also be converted into an "*estimated* number of equivalent QP layers" (although there are no real layers) defined as

$$N = \phi^0_{\mathrm{QP}} h_c / h_p,$$

where h_p =10 nm is the QP thickness and $\phi^0_{\mathrm{QP}} = 0.5$ is an average estimated QP volume fraction inside the assembly.

Results of theoretical calculations of h_c and N with eq. (13) are reported in Fig. 3 together with observations from MC simulations. When considering a fixed subpixel potential of 7 V (Fig. 3a) the predictions at the edge and center of charged regions are in very good agreement with the maximum thickness observed in MC simulation for small and large radii, respectively, as expected from Fig. 2a. For a small particle radius fixed at 10 nm (Fig. 3b) theory also confirms that no assembly should be observed for subpixel potentials below 1 V and that assembly should occur only on charged region edges for larger subpixel potentials. A comparison to experiments with quantum plates will be discussed later on.

Interestingly, an analytical solution for the assembly height as a function of every process parameter can be found at the corner of a square charged region, when $l/L = 1/2$. With $\bar{x} = \bar{z} = 1/2$, equation (12) reduces to

$$\vec{E}|_{\theta=1/2}(\bar{x}=\bar{z}=1/2) = \sum_{p=0}^{\infty} e^{-(2p+1)\pi\bar{y}} \begin{bmatrix}1\\0\\1\end{bmatrix} = \frac{e^{\pi\bar{y}}}{e^{2\pi\bar{y}}-1}\begin{bmatrix}1\\0\\1\end{bmatrix}. \quad (14)$$

Equating the electrostatic and thermal energies as in eq. (13) then yields

$$4\pi\epsilon K a^3 \frac{A^2}{l^2} \frac{e^{2\pi h_c/l}}{(e^{2\pi h_c/l}-1)^2} = \eta k T. \quad (15)$$

Keeping in mind the exponential term is larger than one, this equation has a unique real solution

$$e^{2\pi h_c/l} = \alpha + 1 + \sqrt{\alpha(\alpha+2)} \quad (16)$$

where

$$\alpha = \frac{2\pi\epsilon K a^3 A^2}{\eta k T l^2} \quad (17)$$

is a dimensionless number comparing interaction and thermal energy scales. The deposit height at the corner of a square charged region then reads

$$h_c = \frac{l}{2\pi} \ln\left[\alpha + 1 + \sqrt{\alpha(\alpha+2)}\right] \quad (18)$$

This analytical result is reported in Fig. 3. It does not account for the real maximum assembly height quantitatively, as the latter is rather found either on the edges or at the center of charged regions, but it presents nonetheless a useful qualitative trend.

In particular, equation (18) helps to understand the factors limiting the assembly height. For hypothetical assemblies obtained in the limit $\alpha \ll 1$, i.e. when the interaction energy is barely able to overcome thermal energy, the assembly height becomes

$$h_{c|\alpha\ll1} = \sqrt{\frac{\epsilon K a^3 A^2}{\pi\eta k T}}. \quad (19)$$

This result is reported as a dotted line at small a in Fig. 3a and is indistinguishable from the general solution (18) in Fig. 3b. Interestingly, in this case the assembly height is linear with the surface potential A and scales as $a^{3/2}$ and $(\epsilon K)^{1/2}$. The choice of solvent and nanoparticle material only influences the assembly height weakly because of the constraint $\epsilon < \epsilon_s$ to obtain attractive DEP forces, because $K \leq 1$, and because the exponent $1/2$ is weak. However, the subpixel potential and nanoparticle size can be important levers to control the assembly height. Note that nanoparticles with light conversion capabilities are quite small, with dimensions smaller than a few tenth of nm. In their case, the asymptotic solution (19) is always valid for realistic surface potentials.

For assemblies with strong interactions, which is typical for assemblies of large colloids (namely the case $\alpha \gg 1$), the assembly height (18) can be approximated by

$$h_{c|\alpha\gg1} = \frac{l}{2\pi}\ln 2\alpha = \mathrm{const} + \frac{l}{\pi}\ln A + \frac{3l}{2\pi}\ln a + \frac{l}{2\pi}\ln \epsilon K \quad (20)$$

This relation is reported as a dotted line at large a in Fig. 3a and is not relevant for the conditions of Fig. 3b. For large particles the control parameters A, a, and ϵK do not have as strong effects as for systems of small particles. If technologically acceptable, increasing the charged region size l should be more efficient to increase the assembly height.

Experiments with monodisperse red emitting CdSeS/CdS/ZnS core-shell-shell quantum plates (QP) of dimensions 10 nm×20 nm×20 nm suspended in octane have then been conducted. The nano-objects have been synthesized following the method of Ithurria and Dubertret [32] and have been used recently in a photolithography process to build a color conversion layer for micro-display applications [33, 25]. Here, subpixel potentials between 2 and 9 V, and subpixel arrays with $l/L = 1/2$ and L = 5, 10, and 15 µm have been tested. First, charges were injected to create a 5×5 subpixel array in a 500 nm thick PMMA substrate with an AFM, applying varying potentials on the tip depending on the desired subpixel potential. Charge injection was performed using 1 ms pulses at 50 Hz in tapping mode with a 10 µm s^{-1} tip speed inducing tiny charged dots (theoretically 10 nm wide charged points spaced by 190 nm distance). After charge injection, the surface potential map was measured by Amplitude Modulation Kelvin Probe Force Microscopy (AM-KFM) (Fig. 4a) and 1D profiles have been extracted to measure the actual average subpixel potential and its variability from subpixel to subpixel (Fig. 5). Note that AM-KFM measurements in our conditions at a 50 nm lift height are not resolute enough to discriminate the discrete charge points due to parasitic capacity effects [34, 35].

A 20 µL drop of suspension of quantum plates dispersed in octane was then deposited on the subpixel array for 10 s, and the substrate was dipped for 5 minutes in pure octane without

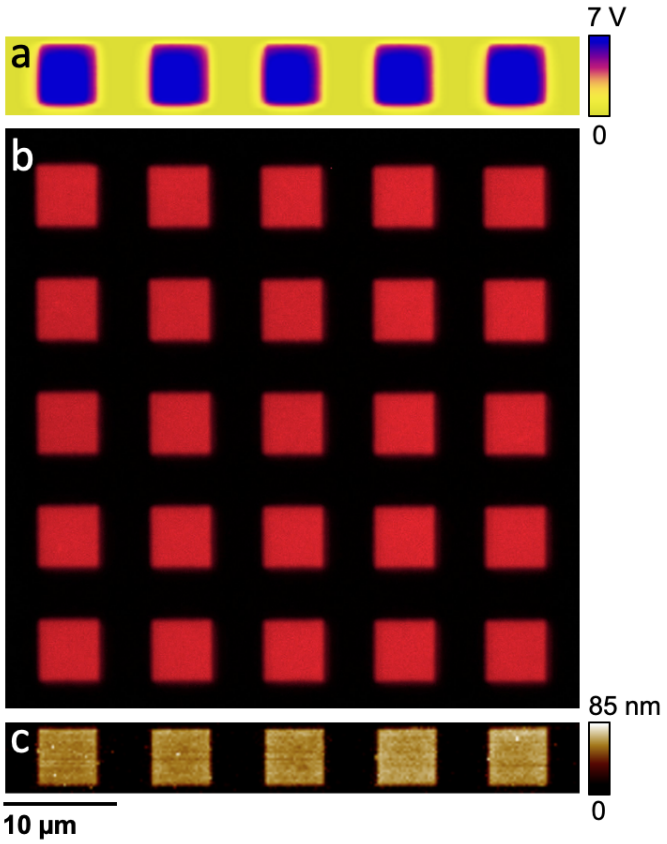

Figure 4: Experimental data collected for a quantum plate assembly experiment with AFM charge injection at 55 V, charged region dimensions $l_x = l_y = 5\,\mu$m and pitch $L_x = L_z = 10\,\mu$m. a: surface potential scan performed by AM-KFM just after charge injection and before QP assembly. b: photoluminescence image (450 nm, 58 ms exposure time) after QP assembly on a 5×5 subpixel array, showing good uniformity. c: AFM topography scan performed over one row of subpixels.

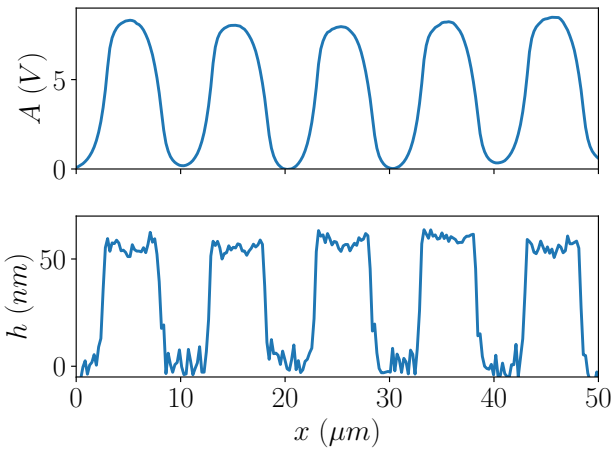

Figure 5: Top: 1D AM-KFM surface potential scan before QP assembly. Bottom: 1D AFM topography scan performed after QP assembly. These data are extracted from the 2D scans reported in Fig. 4a and 4c.

agitation before any evaporation-induced assembly could occur in the quickly drying drop. The substrate was then left to dry in air. Without such a protocol, the suspension drop would quickly evaporate and the excess, non-assembled, colloids still in the droplet would be forced to assemble on the substrate by convective assembly taking place at the receding contact line [36]. This may help enhance electrostatic assembly if performed at adequate rates [37] but it would prevent comparison between the experiments and the models presented in this work. During immersion in pure octane, the excess colloids are allowed to diffuse away from the substrate, and the final drying step then involves only pure solvent. Photoluminescence images were then taken, revealing selective directed assemblies located exactly over the charged subpixels (Fig. 4b). As anticipated, assembly occurred on the entire surface of each charged region and not only on its edges as in the simulations reported in Fig. 2b. AFM topography measurements were then undertaken (Fig. 4c) and 1D thickness profiles were used to obtain the average assembly height and its variability (Fig. 5). These measurements reveal a rather uniform QP assembly over the full charged region surface, which can be explained if the discrete charge injection points have sharp boundaries, such as those reported for example in [38]. Indeed, in this case the sub-array of injections points within a charged region may by considered as a sub-pattern of smaller charged regions with periodicity L =100–200 nm and lateral extent, say, $l \sim 50$ nm. For the assembly of small nano-objects, relation (19) can be applied to the tiny sub-pattern defined by charged dots and, interestingly, this relation depends on neither L nor l. This means that the critical assembly height over the edge of each one of the injection points within a charged region is the same as the one predicted on the edge of a micron-sized, uniformly charged region. Of course, the injection points are not squares with infinitely sharp boundaries but we believe nonetheless that this picture explains why experimental charged regions are entirely filled by QP and with a uniform QP thickness.

The thickness of experimental quantum plate assemblies performed for different subpixel potentials and different charged region sizes is compared to theory and simulation results in Fig. 3b. As expected, we can observe a quite good agreement between the experimental QP thickness and the thicknesses predicted by MC simulations and theory on the edge of charged regions. Besides, the value of L has no clear influence in experiments, as predicted by relation (19).

To summarize briefly, the joint examination of theory, MC simulation results and experiments allows to conclude that (i) the nonuniform charge distribution inside charged regions is responsible for the uniform assembly of nanoparticles over the whole charged region surface, (ii) the assembly thickness can be predicted semi-quantitatively by solving eq. (13) on the edge of a charged region ($x = l/2$, $z = 0$) and good orders of magnitude are provided by the analytical solution at a charged region corner (18) or the more explicit relation (19) valid for semiconductor nanocrystals.

With this last conclusion at hand, anticipating possible assembly thicknesses as a function of nano-object size a and subpixel potential A becomes possible, as shown in Fig. 6. For radii

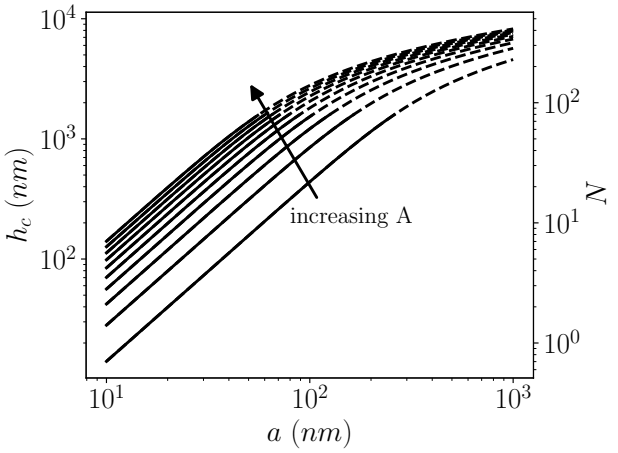

Figure 6: Thickness h_c of the assembly at a square charged region corner for $l/L = 1/2$ (eq. (18)) as a function of nanoparticle radius and for increasing surface potentials. The subpixel potential A is varied between 2 V and 20 V by steps of 2 V. The fixed parameters used here are those reported in Table 1. Lines are dashed when neighbouring assemblies have grown enough laterally to merge.

smaller than 100 nm the $a^{3/2}$ behavior relevant in the $\alpha \ll 1$ limit (19) of small objects is valid for any realistic value of the subpixel potential. Note that nanoparticles with light conversion capabilities have dimensions smaller than 10–20 nm so they invariably fall in this domain. Moreover, in their case Fig. 6 shows that increasing the subpixel potential even to 20 V, which may not even be possible in practice, can only lead to assembly thicknesses lower than 200 nm, which is consistent with recent assembly attempts [10, 25]. Recent photo-luminescence measurements performed on 150 nm assemblies showed an external quantum yield of 7.5% [25]. This corresponds to roughly $N = 7.5$ equivalent QP layers. Extrapolating this result linearly, in particular ignoring reabsorption and scattering phenomena, we can estimate that the minimum assembly thickness to obtain 95% color conversion should be around 1.9 µm, or $N \simeq 95$ equivalent QP layers. Since the assembly height is linear with the subpixel potential, one can extrapolate that to get satisfactory color conversion properties the subpixel potential used for QP assembly should be of the order of 100–200 V, which is definitely not realistic.

This leads us to the conclusion that dielectrophoretic assembly applied directly to small quantum dots or quantum plates cannot be used to achieve the desired light conversion efficiency, at least in the present form. Fig. 6 suggests that thick enough deposits could be obtained by assembling larger colloids that would embed semiconductor nanocrystals. Possible candidates are quantum dot or quantum plate aggregates, or hybrid metal oxide colloids embedding several light emitters on their surface [39] or inside their core [6]. Assembling such objects however raises two new issues discussed in the next section: first, the dilution of QPs inside these objects automatically imposes that assemblies will need to be thicker to get the same number of equivalent QP layers, and second, higher assemblies are inherently wider, possibly even merged, which imposes a constraint on the minimal pixel size addressable by nanoxerography.

3. Assembly of large monodisperse colloids embedding quantum plates

When quantum plates are embedded into larger objects, such as metal oxide spheres or aggregates, a deposit with a larger thickness may be required to have the same optical conversion due to the dilution of QPs inside these larger colloids, and due to the voids left between them. Let the volume fraction of large colloidal carriers in an assembly be $\phi_C \simeq 0.7$ and the volume fraction of QPs inside one of them be ϕ_{QP}. The number of equivalent QP layers in a colloidal carrier assembly of height h is

$$N = \phi_C \phi_{QP} h / h_p.$$

Therefore, if a photon needs to encounter $N \simeq 95$ QP layers for 95% color conversion efficiency, then the assembly height should be at least 3.4 µm for metal oxide spheres loaded at, say, $\phi_{QP} \simeq 0.4$. In the most optimistic case, the colloidal carriers would be close packed QP aggregates with a volume fraction close to unity, and the minimal assembly height would be 1.3 µm. Note however that such close-packed stacks seem to reduce the QP quantum yield [40, 41]. So in practice, the targeted assembly thickness when using colloidal carriers is a few microns. According to Fig. 6 such a thickness can be obtained for 5 micron wide charged region with realistic subpixel potentials (< 10 V) and micro-pearls with a radius larger than about 200 nm.

However, the new issue of controlling the lateral extent of assemblies will now have to be faced: simulations show that higher assemblies also tend to get wider, with the assembly half-width w becoming larger than the charged region width l, and up to a point where colloidal assemblies centered over neighbouring subpixels even start to merge ($w > L/2$, see Fig. 2a for the largest radius, and the dashed lines in Fig. 6). In display applications, R/G/B subpixels are alternated so too large an assembly could lead to a form of cross-talk by deposition of red-emitting nanoparticles over green and blue emitting subpixels for example. If the assembly half-width w is constrained to be smaller than a given value to avoid cross-talk, reducing the charged region width l, for a fixed pitch L, would be a straightforward solution, but this will automatically reduce the assembly height. A compromise needs to be found to get a high-enough assembly for efficient color conversion while avoiding cross-talk.

The possible merging of assemblies over neighboring charged regions is illustrated more quantitatively in Fig. 7 as a function of the position $\{a, A, l\}$ in the parameter space. Here we consider a monochrome array of square subpixels with $l/L = 1/2$ for simplicity. The charged region width is fixed at $l = 15$ µm in Fig. 7a, and the color map shows the estimated number of equivalent QP layers N increases with colloid size a and subpixel potential A as described above. The red dashed line delimits the acceptable domain in terms of color conversion

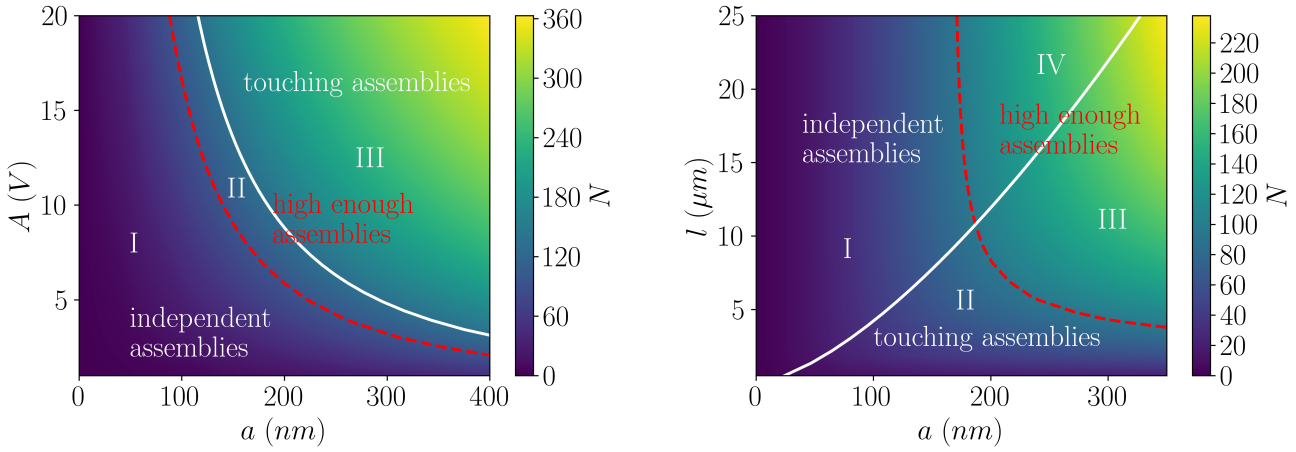

(a) $l = 15\,\mu m$.

(b) $A = 7\,V$.

Figure 7: Color maps representing the estimated number of equivalent QP layers N at a square charged region corner with $l/L = 1/2$. White line: boundary between the parameter regions in which independent or merged assemblies are obtained. Red dashed line: boundary delimiting the parameter region in which high enough assemblies are obtained.

($N \gtrsim 95$), i.e. regions II and III. The white line delimits the regions where assemblies centered over neighboring charged regions merge or not. Non-touching assemblies are obtained only in regions I and II. Therefore only region II of the parameter space can be used for display applications. This region appears quite narrow but it depends on the charged region width l, as becomes clear in Fig. 7b. Here the estimated number of equivalent QP layers N is represented as a function of a and l for $A = 7$ V: larger colloids and larger charged areas allow higher (and wider) assemblies. The allowed parameter region is now only region IV. The important piece of information from Fig. 7b is that region IV does not reach small subpixel sizes. Specifically, assemblies with satisfactory color conversion capability will always merge below $l \simeq 10\,\mu m$ for $A = 7$ V, independently of the colloid size. This result simply states that the aspect ratio h/w of the assembly built using DEP driven assembly cannot be too high. As discussed in Supplementary Material, similar maps for $A = 4$ and 10 V show that the limit $l \simeq 10\,\mu$m seems to be independent of A, and the white line delimiting the merged/non-merged subpixel regions in Fig. 7a seems to match with iso-h levels. This would suggest the shape of the assemblies could be self-similar.

The height of an assembly above the edge of the charged region h_e and the estimated number of equivalent QP layers at the edge N are reported as a function of the lateral assembly extent beyond $l/2$ in Fig. 8. These quantities are indeed proportional to a large extent, with $h_e \simeq 1.125(w - l/2)$ here. Every curve departs from this law when a and A attain their highest values, with the assembly width increasing faster than the assembly height. This phenomenon is less pronounced when l/L decreases (not shown) so it may be the signature of neighboring charged regions helping to capture colloids over a given central charged region. This feature is actually quite marginal and the lateral extent of assemblies beyond $l/2$ is indeed essentially proportional to their height. Because assemblies obtained by DEP

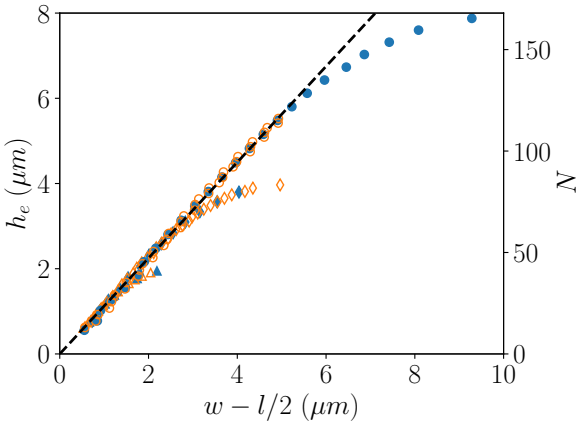

Figure 8: Assembly height h_e at the edge of a charged region and estimated number of equivalent QP layers at the edge N as a function of the lateral extent of an assembly beyond the edge of the charged region for monodisperse suspensions. △: l =5 μm; ◇: l =10 μm; ○: l =20 μm. Blue filled symbols: variation of a between 10 and 400 nm with $A = 7$ V. Orange open symbols: variations of A between 1 and 20 V with $a = 100$ nm. Other fixed parameters are $L = 2l$, $\epsilon = 1.95\epsilon_0$, $\epsilon_s = 9\epsilon_0$.

will inherently have this self-similar shape, a trade-off will always exist exist between light emitter density at the subpixel center and lateral cross-talk. This self-similar shape is also the reason why the l =10 μm limit seems independent of the subpixel potential: indeed, if a high enough thickness is chosen, then the assembly extent beyond the charged region limit will also be fixed, whatever the value of A used to attain this desired thickness.

These conclusions suggest that assembling colloids with radii in the range 200–300 nm over sufficiently large charged regions ($l \gtrsim 10\,\mu$m) can indeed allow for enough QP to be gathered over subpixels to achieve the color conversion perfor-

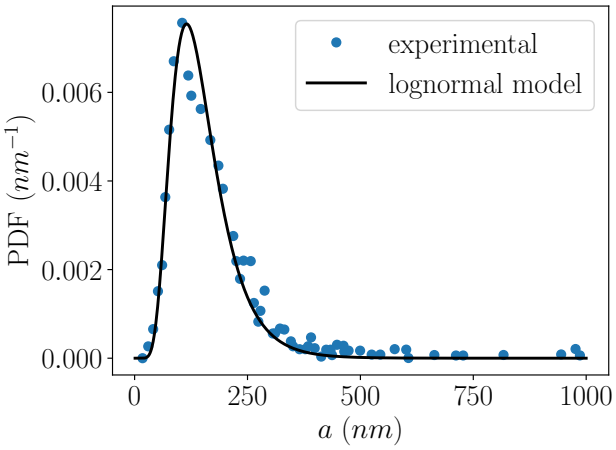

Figure 9: Distribution of radii in a micro-pearl suspension synthesized by NEXDOT. The data was acquired using dynamic light scattering.

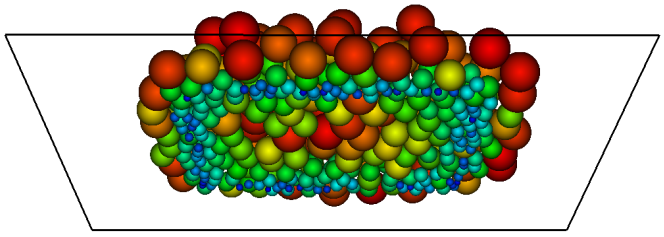

Figure 10: Snapshot taken from below the substrate in a Monte Carlo simulation of micro-pearl assembly. The colloids are colored after their radius.

mances targeted for next-generation displays. These conclusions are based on a theoretical model for monodisperse colloidal spheres, whereas actual colloidal QP carriers, such as metal oxide beads or QP aggregates, are expected to be quite polydisperse in practice. In the next section, we discuss the results of experiments involving polydisperse alumina spheres encapsulating quantum plates, as well as the corresponding GCMC simulations, in light of the theoretical conclusions.

4. Assembly of quantum-plate-embedding alumina spheres

Hybrid colloids encapsulating quantum plates in an alumina matrix, termed micro-pearls here, have been synthesized using a patented process by NEXDOT to improve the QP chemical, physical and photo stability. The micro-pearls were dispersed in heptane at a concentration of approximately 1 mg mL^{-1}, so the bulk volume fraction of micro-pearls was about 2×10^{-4}. The micro-pearls are spherical but quite polydisperse with radii ranging essentially from 10 to 300 nm and a tail of larger objects (see Fig. 9). The radii distribution is well approximated by a log-normal distribution with maximum probability density around $a = 120$ nm.

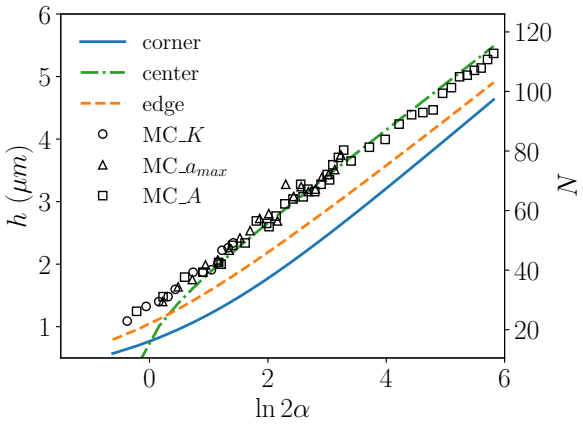

Figure 11: Assembly height h and estimated number of equivalent layers N on a charged region in Monte Carlo simulations of micro-pearls assembly (black open symbols), and as predicted by theory at the corner, edge, and center of a charged region (lines). Unless specified otherwise, the parameters used here are those reported in table 1. For simulations MC_K, $A = 0.7\,V$ and ϵ_s is varied between 3 and 64 so K is between 0.15 and 0.91. For simulations MC_$a_{\max}$, $A = 1\,V$ and $a_{\max}$ is varied between 220 and 600 nm. For simulations MC_A, A is varied between 0.4 and 10 V.

A snapshot of a Monte Carlo simulation of micro-pearl assembly is reported in Fig. 10. Size segregation is quite evident: the smallest colloids are located closest to the charged region edge, where the electric field gradient is the largest, whereas the upper and outer layers of the assembly are constituted mainly by the largest colloids. This segregation is due to the effective dipole moment being proportional to a^3, so the smallest colloids are captured only in regions with the most intense field gradients, and the largest colloids can be captured in regions of relatively weak ∇E^2. From this picture and the energetic argument behind eq. (13), it is expected that the maximum assembly height is given by the maximum assembly height of a monodisperse suspension with the maximum micropearl radius $a_{\max}$. This assembly height is reported as a function of $\ln 2\alpha$ in Fig. 11 for simulations with varying micropearl dielectric constants, maximum micropearl radii, and subpixel potentials. The good collapse of all the simulation results over a single master curve shows that the assembly height varies indeed as $\ln 2\alpha$, as predicted by relation (20), although this relation was derived at the corner of a charged region and for a monodisperse suspension. Moreover, these results can be predicted accurately with the semi-analytical solution of eq. (13) at a subpixel center, as expected for these large colloids (see the green dot-dashed line in Fig. 11), and the number of equivalent QP layers can indeed exceed 95 as targeted. The important point about these simulation results is that the theory for monodisperse suspensions underlying the useful predictions (18)-(19)-(20) and used to build the maps in Fig. 7 can be extended to polydisperse suspensions by considering the maximum colloid radius allowed in the size distribution as the radius used in the monodisperse theory.

The maps reported in Fig. 7 suggest that good subpixel assemblies could be obtained for $A = 7$ V, $l = 15\,\mu$m, $L = 30\,\mu$m

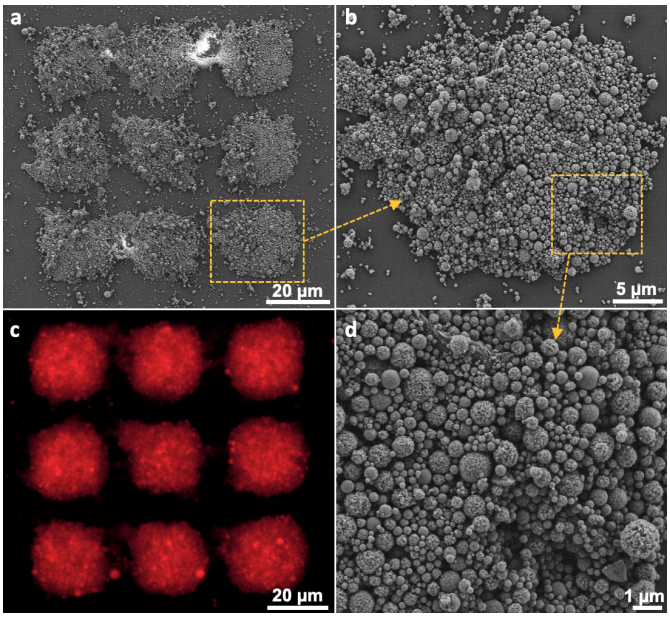

Figure 12: Micro-pearl assemblies on 15 µm charged regions: SEM at 3 magnifications (a, b, d) and photo-luminescence (c). The time of contact between the micropearl dispersion and the substrate was 16 seconds.

and colloidal carrier radii around 200 nm. An assembly experiment similar to the one performed on independent quantum plates has then been attempted with micro-pearls in these conditions. The thickness of micropearl assemblies increased progressively with time and could reach several micrometers. Well defined assemblies could be observed during an initial period of time, as reported in Fig. 12. However, neighboring assemblies then began to merge for longer development times and assembly thicknesses larger than 5 µm, with very large micron-sized micro-pearls assembling quite far away from the charged region (see Supplementary Material). This is consistent with the maps in Fig. 7 showing that colloids with radii larger than about 240 nm will assemble into merged structures. This experiment highlights an important point for applications: colloidal carriers need to be synthesized with a quite narrow size distribution to avoid assembly merging. The recommended strategy to get well defined, independent assemblies with enough equivalent QP layers for successful color conversion is thus to (i) embed light emitting nanocrystals into larger colloidal carriers, (ii) maximize the volume fraction of nanocrystals inside the carriers so the assembly thickness, and thus the assembly width, is minimized, (iii) make the size polydispersity of carriers as narrow as possible to avoid assembly merging due to the remote assembly of the largest carriers. In view of these elements, a promising route could be to produce quite monodisperse quantum plate aggregates in the form of close packed stacks if the quantum yield decay associated to the stacking could be controlled.

5. Conclusion

Theory, simulations, and experiments on the electrostatic directed assembly of semiconductor nanocrystals on a substrate patterned by nanoxerography have been presented with a view to designing a new protocol for the fabrication of next-generation quantum dot or quantum plate displays.

We first investigated the case of direct, patterned quantum plate assembly to understand why the number of quantum plates deposited per unit surface area was always much too low for applications in recent assembly attempts [10, 25]. The main reason is that the small size of light-emitting nanocrystals confers them only very small effective dipole moments, so dielectrophoretic forces quickly become weaker than thermal forces at distances from the substrate of the order of 100-200 nm. The other process parameters cannot be tuned to improve this significantly.

From theory and simulation results, we showed that larger colloidal objects embedding quantum plates could be assembled to form color conversion layers with enough light emitters per unit surface area for applications. Possible options are quantum plate aggregates, or metal oxide spheres embedding quantum plates inside them or on their surface. However, we also showed that this increase of the number of assembled colloidal objects was associated to a widening of the assemblies, which may lead to cross-talk between adjacent subpixels. Patterned assembly of semiconductor nanocrystals by nanoxerography is thus not applicable for subpixel sizes below 10-20 microns.

To validate these theoretical and numerical predictions, we assembled 100-300 nm metal oxide spheres embedding quantum plates (micro-pearls) over an array of 15 µm subpixels. During the process, the thickness of the assembly increased progressively up to 5 µm after what neighboring assemblies started to merge. This issue was due to to the largest and rarest micro-pearls being able to assemble far away from pixel centers. These experiments brought two main conclusions: first, very thick assemblies can indeed be formed using larger colloidal carriers in the conditions predicted by theory and second, the suspensions of quantum plate carriers should be quite monodisperse to avoid uncontrolled merging of neighbouring assemblies.

The results from this work suggest that the perspectives to improve the process of building patterned color conversion layers by nanoxerography actually concern the design of the colloidal carrier suspensions. Indeed, the colloidal vectors should embed as much semiconductor nanocrystals as possible to minimize the thickness and lateral extent of the assemblies formed over each subpixel. Good candidates are thus micro-pearls with very high quantum plate density or simply quantum plate aggregates. The maximum size of colloidal carriers should also be controlled precisely either during synthesis, which may be challenging, or by using a size separation technique to remove the large size tail of the distribution.

Acknowledgements

This work was supported by the Agence Nationale de la Recherche (ANR) (Grant ANR-20-CE09-0019-02). It was performed using HPC resources from GENCI-TGCC/IDRIS (grant A0110911444) and CALMIP (project P21039).

References

[1] H. Chen, J. He, S.-T. Wu, Recent advances on quantum-dot-enhanced liquid-crystal displays, IEEE Journal of Selected Topics in Quantum Electronics 23 (5) (2017) 1–11.

[2] Y.-M. Huang, K. J. Singh, A.-C. Liu, C.-C. Lin, Z. Chen, K. Wang, Y. Lin, Z. Liu, T. Wu, H.-C. Kuo, Advances in quantum-dot-based displays, Nanomaterials 10 (7) (2020) 1327.

[3] M. A. Triana, E.-L. Hsiang, C. Zhang, Y. Dong, S.-T. Wu, Luminescent nanomaterials for energy-efficient display and healthcare, ACS Energy Letters 7 (3) (2022) 1001–1020.

[4] Y. E. Panfil, M. Oded, U. Banin, Colloidal quantum nanostructures: emerging materials for display applications, Angewandte Chemie International Edition 57 (16) (2018) 4274–4295.

[5] Z. Liu, C.-H. Lin, B.-R. Hyun, C.-W. Sher, Z. Lv, B. Luo, F. Jiang, T. Wu, C.-H. Ho, H.-C. Kuo, et al., Micro-light-emitting diodes with quantum dots in display technology, Light: Science & Applications 9 (1) (2020) 83.

[6] M. Yu, M. H. Saeed, S. Zhang, H. Wei, Y. Gao, C. Zou, L. Zhang, H. Yang, Luminescence enhancement, encapsulation, and patterning of quantum dots toward display applications, Advanced Functional Materials 32 (13) (2022) 2109472.

[7] E. Palleau, N. M. Sangeetha, G. Viau, J.-D. Marty, L. Ressier, Coulomb force directed single and binary assembly of nanoparticles from aqueous dispersions by afm nanoxerography, Acs Nano 5 (5) (2011) 4228–4235.

[8] E. Palleau, L. Ressier, Combinatorial particle patterning by nanoxerography, Advanced Functional Materials 28 (30) (2018) 1801075.

[9] X. Xing, Z. Man, J. Bian, Y. Yin, W. Zhang, Z. Lu, High-resolution combinatorial patterning of functional nanoparticles, Nature communications 11 (1) (2020) 6002.

[10] C. Midelet, G. Petit, S. Raffy, Y. Hallez, S. M. Marinho, M. Pousthomis, M. d'Amico, F. Guérin, E. Palleau, L. Ressier, On the in situ 3d electrostatic directed assembly of cdse/cdzns colloidal quantum nanoplatelets towards display applications, Journal of Colloid and Interface Science 630 (2023) 924–933.

[11] D. Poirot, R. Platel, T. Alnasser, F. Guerin, E. Palleau, L. Ressier, Smartphone-identifiable photoluminescent nanoparticle-based multilevel secured tags by electrical microcontact printing, ACS Applied Nano Materials 1 (10) (2018) 5936–5943.

[12] L. Teulon, E. Palleau, D. Morales, D. Poirot, L. Ressier, Interactive nanogel marking at the microscale for security and traceability applications, Advanced Materials Technologies 3 (2) (2018) 1700244.

[13] M. Kolibal, M. Konecny, F. Ligmajer, D. Skoda, T. Vystavel, J. Zlamal, P. Varga, T. Sikola, Guided assembly of gold colloidal nanoparticles on silicon substrates prepatterned by charged particle beams, ACS nano 6 (11) (2012) 10098–10106.

[14] H. Fudouzi, M. Kobayashi, N. Shinya, Site-controlled deposition of microsized particles using an electrostatic assembly, Advanced Materials 14 (22) (2002) 1649–1652.

[15] A. Shahmoon, O. Limon, O. Girshevitz, Z. Zalevsky, Self assembly of nano metric metallic particles for realization of photonic and electronic nano transistors, International Journal of Molecular Sciences 11 (5) (2010) 2241–2252.

[16] H. Fudouzi, M. Kobayashi, N. Shinya¿, Assembling 100 nm scale particles by an electrostatic potential field, Journal of Nanoparticle Research 3 (2001) 193–200.

[17] H. O. Jacobs, G. M. Whitesides, Submicrometer patterning of charge in thin-film electrets, Science 291 (5509) (2001) 1763–1766.

[18] C. R. Barry, J. Gu, H. O. Jacobs, Charging process and coulomb-force-directed printing of nanoparticles with sub-100-nm lateral resolution, Nano letters 5 (10) (2005) 2078–2084.

[19] P. Mesquida, A. Stemmer, Attaching silica nanoparticles from suspension onto surface charge patterns generated by a conductive atomic force microscope tip, Advanced Materials 13 (18) (2001) 1395–1398.

[20] N. Naujoks, A. Stemmer, Micro-and nanoxerography in liquids–controlling pattern definition, Microelectronic Engineering 78 (2005) 331–337.

[21] S.-D. Tzeng, K.-J. Lin, J.-C. Hu, L.-J. Chen, S. Gwo, Templated self-assembly of colloidal nanoparticles controlled by electrostatic nanopatterning on a si3n4/sio2/si electret, Advanced Materials 18 (9) (2006) 1147–1151.

[22] L. Seemann, A. Stemmer, N. Naujoks, Selective deposition of functionalized nano-objects by nanoxerography, Microelectronic engineering 84 (5-8) (2007) 1423–1426.

[23] L. Seemann, A. Stemmer, N. Naujoks, Local surface charges direct the deposition of carbon nanotubes and fullerenes into nanoscale patterns, Nano letters 7 (10) (2007) 3007–3012.

[24] L. Ressier, E. Palleau, C. Garcia, G. Viau, B. Viallet, How to control afm nanoxerography for the templated monolayered assembly of 2 nm colloidal gold nanoparticles, IEEE transactions on nanotechnology 8 (4) (2009) 487–491.

[25] E. Yassitepe, P. Tyagi, E. Palleau, S. Raffy, A. Cuche, S. Poncet, J.-C. Pillet, S. Altazin, F. Guérin, Y.-P. Lin, M. D'Amico, L. Ressier, Combinatorial patterning of red- and green-emitting core-shell cd(se,s)/(cd,zn)s quantum nanoplatelets for high-resolution color-converter microdisplays, ACS Applied Nano Materials (2024). doi:10.1021/acsanm.4c02989.

[26] P. Moutet, P. Deram, N. M. Sangeetha, L. Ressier, Dynamics of dielectrophoretic-force-directed assembly of nayf4 colloidal nanocrystals into tunable multilayered micropatterns, The Journal of Physical Chemistry Letters 5 (17) (2014) 2988–2993.

[27] T. B. Jones, Electromechanics of Particles, Cambridge University Press, 1995. doi:10.1017/CBO9780511574498.

[28] R. R. Pethig, Dielectrophoresis: Theory, methodology and biological applications, John Wiley & Sons, 2017.

[29] Y. Hallez, J. Diatta, M. Meireles, Quantitative assessment of the accuracy of the poisson–boltzmann cell model for salty suspensions, Langmuir 30 (23) (2014) 6721–6729.

[30] Y. Hallez, M. Meireles, Modeling the electrostatics of hollow shell suspensions: Ion distribution, pair interactions, and many-body effects, Langmuir 32 (40) (2016) 10430–10444.

[31] J. N. Israelachvili, Intermolecular and surface forces, Academic press, 2011.

[32] S. Ithurria, B. Dubertret, Quasi 2d colloidal cdse platelets with thicknesses controlled at the atomic level, Journal of the American Chemical Society 130 (49) (2008) 16504–16505.

[33] E. Quesnel, A. Suhm, M. Consonni, M. Reymermier, G. Lorin, C. Laugier, M. Tournaire, P. Le Maitre, A. Lagrange, B. Racine, et al., Experimental and theoretical investigation of 2d nanoplatelet-based conversion layers for color led microdisplays, Optics Express 29 (13) (2021) 20498–20513.

[34] E. Palleau, L. Ressier, T. Mélin, et al., Numerical simulations for a quantitative analysis of afm electrostatic nanopatterning on pmma by kelvin force microscopy, Nanotechnology 21 (22) (2010) 225706.

[35] F. Pertl, J. C. Sobarzo, L. Shafeek, T. Cramer, S. Waitukaitis, Quantifying nanoscale charge density features of contact-charged surfaces with an fem/kpfm-hybrid approach, Physical Review Materials 6 (12) (2022) 125605.

[36] L. Malaquin, T. Kraus, H. Schmid, E. Delamarche, H. Wolf, Controlled particle placement through convective and capillary assembly, Langmuir 23 (23) (2007) 11513–11521.

[37] L. Teulon, Y. Hallez, S. Raffy, F. Guerin, E. Palleau, L. Ressier, Electrostatic directed assembly of colloidal microparticles assisted by convective flow, The Journal of Physical Chemistry C 123 (1) (2018) 783–790.

[38] N. Knorr, S. Vinzelberg, Charge writing and detection by efm and kpfm scanning probe techniques, Microscopy and Analysis 26 (5) (2012).

[39] R. Platel, L. Vaure, E. Palleau, S. Raffy, F. Guerin, D. Lagarde, R. Cours, C. Marcelot, B. Warot-Fonrose, C. Nayral, et al., Synthesis of hybrid colloidal nanoparticles for a generic approach to 3d electrostatic directed assembly: application to anti-counterfeiting, Journal of Colloid and Interface Science 582 (2021) 1243–1250.

[40] B. Guzelturk, O. Erdem, M. Olutas, Y. Kelestemur, H. V. Demir, Stacking in colloidal nanoplatelets: tuning excitonic properties, ACS nano 8 (12)

(2014) 12524–12533.
[41] S. Jana, T. N. Phan, C. Bouet, M. D. Tessier, P. Davidson, B. Dubertret, B. Abécassis, Stacking and colloidal stability of cdse nanoplatelets, Langmuir 31 (38) (2015) 10532–10539.